JOURNAL OF AIRCRAFT
Vol. 40, No. 4, July–August 2003

Analytic Prediction of Surface Pressures over a Hemisphere-Cylinder at Incidence

Lance W. Traub* and Othon Redinioti†
Texas A&M University, College Station, Texas 77843-3141

The utility of the hemisphere cylinder configuration lends itself to widespread application, ranging from measurement probes to underwater vehicles. A simple explicit method to estimate the surface pressures over this configuration would be of use for both conceptual design and for understanding the relation of the design variables. Consequently, an explicit equation is developed that requires only the hemisphere cylinder incidence and the location of the point of interest to yield the final surface flow. Surface pressures are calculated using perturbation potentials calculated from least-square curve fits to numerically estimated potentials. Comparisons of the expression with experimental data show good agreement.

Nomenclature

C_P = pressure coefficient
f^e = source ring strength
K^e = kernel function
k = geometric parameter
l = body length
P_n = source ring influence parameter
R = hemisphere radius
r = orthogonal coordinate
U = freestream
V_θ = tangential velocity
W = transverse velocity
w_1 = lateral velocity
w_2 = axial velocity
x, y, z = Cartesian coordinates, origin at hemisphere nose
x', y, z = Cartesian coordinates, origin at hemisphere-cylinder juncture
α = geometric parameter
θ = spherical coordinate angle, measured from nose of hemisphere
θ_H = hemisphere cylinder incidence angle
θ_V = angle to the point of interest measured from the attachment line
λ = geometric parameter
ρ, ζ = orthogonal coordinates
ϕ = potential
ϕ' = perturbation potential

Introduction

THE wide range of applications of the hemisphere-cylinder (H-C) configuration has led to numerous investigations to elucidate its aerodynamic characteristics. H-C's form the baseline shape of many underwater vehicles, subsonic missiles as well as measurement probes. Both experimental[1–3] and numerical[4] studies have clarified effects of incidence and Reynolds number on surface pressure loads and on- and off-surface flow topology. Generally, at low incidence for $-15 < \theta < 15$ deg, the effect of the cylinder on the surface pressures over the hemisphere is marginal, such that the flow resembles that over a sphere. Note that $\theta = 0$ deg indicates the H-C nose, and $\theta = 90$ deg the H-C junction. For larger θ the source-like effect of the cylinder results in reduced tangential velocities compared to the sphere. At zero incidence in the laminar subcritical range, the minimum recorded pressures for the H-C generally occur[1] at $\theta \approx 67(Re = 2{\cdot}7 \times 10^4) - 76(Re > 2{\cdot}9 \times 10^5)$ deg compared to $\theta \approx 72$ deg for a sphere[5] ($Re = 16{\cdot}3 \times 10^4$). At these Reynolds numbers the minimum recorded pressure coefficient for the H-C is typically $\approx -0{\cdot}64$ while that for a sphere is $\approx -0{\cdot}56$. Increasing the Reynolds number past critical shows an aft movement of the point of minimum pressure with a concomitant increase in the minimum pressure attained.

Viscous effects have a pronounced effect on the flow behavior over a H-C. At low incidence pressure recovery at the intersection of the hemisphere with the cylinder generally causes localized flow separation in the form of a ring-shaped bubble.[1] Turbulent transition generally closes the separation. As the incidence of the H-C increases, the separation region looses axisymmetry and moves from the windward side toward the leeward side of the H-C. A localized separation bubble may still exist on the leeward surface at $x/R \approx 1$; however, it may terminate in two unstable foci, which mark the liftoff location for two "horn vortices." Further down the cylindrical body, crossflow separation also results in the formation of vortices (which may connect with the aforementioned horn vortices). This vortex formation is dependent on the state of the crossflow boundary layer and hence Reynolds number. Consequently, the flow over a H-C at incidence can be considered to be constituted of both potential (windward) and viscous flow regions (leeward) with the boundaries determined by the operating conditions, e.g., incidence, Reynolds number, turbulence, etc. Pointed-nose axisymmetric bodies are prone to asymmetric wake development for large angles of attack. The asymmetry of the vortex wake can be caused by any slight surface perturbation. H-Cs are generally not as prone to vortex asymmetry as sharp axisymmetric bodies; however, a moderately small surface perturbation in the nose vicinity of a H-C can cause asymmetrical vortex development.[1] For H-C incidence angles θ_H greater than 15 deg and less then 42 deg, the wake of the cylinder can also contain unsteadiness. The unsteadiness is caused by periodic heaving of the vortices as they convect downstream.[1] For incidences greater then 42 deg, H-Cs exhibit vortex shedding.[1]

The wide-ranging application of H-C configurations makes it valuable for the designer to have a simple analytic tool that would allow estimates of the surface pressures over a H-C at incidence. Traub[6–9] has shown that analytic prediction methods can offer simplicity and utility to the designer and allow a "feel" for the respective design variables. Consequently, an analytic method has been developed. The method uses the surface singularity methods of Landweber[10] and Lotz[11] to estimate the perturbation potentials for

---

Received 8 October 2000; revision received 10 April 2001; accepted for publication 18 April 2001. Copyright © 2001 by Lance W. Traub and Othon Redinioti. Published by the American Institute of Aeronautics and Astronautics, Inc., with permission. Copies of this paper may be made for personal or internal use, on condition that the copier pay the $10.00 per-copy fee to the Copyright Clearance Center, Inc., 222 Rosewood Drive, Danvers, MA 01923; include the code 0021-8669/03 $10.00 in correspondence with the CCC.

*TEES Research Scientist/Lecturer, Aerospace Engineering Department. Associate Member AIAA.

†Associate Professor, Aerospace Engineering Department. Member AIAA.

axial and transverse flow, respectively. These potentials are then approximated using a least-squares curve fit. Potential theory is then used to develop a final single expression that allows for pressure estimation. An experimental study was also undertaken to provide data for comparison. Numerous theoretical and experimental data comparisons are presented. Agreement is seen to be very good, which is encouraging considering the simplicity of the final analytic expression.

Theoretical Development

As Laplace's equation is linear, the perturbation potential caused by axial flow and that caused by transverse flow can be decomposed and solved independently. For simplicity, different methods were used for the axial and transverse flow solutions. A brief overview of these methods is presented. Specific details can be found in the cited references.

Axial Flow

Initially, the accuracy of surface and axis distributed singularity methods was investigated. Figure 1 shows comparisons (the axis method used doublets; the surface method will be detailed next). It may be seen that for this type of body an axial distribution of singularities does not yield an accurate representation of the flow, essentially caused by a discontinuous second derivative of the surface at the H-C juncture. It was thus decided that the surface singularity method would be used to model the flow despite a significant increase in complexity. The axial flow over the H-C was solved for using the method of Landweber,[10] as presented by Albone.[12] Landweber has shown that by applying Green's theorem to the solution of the boundary-value problem for ϕ an integral expression for the surface velocity can be obtained. Thus, the method consists of solving the integral equation for the surface velocity:

$$\int_0^P \frac{U(x)y(x)^2\,\mathrm{d}s}{2r(x,t)^3} = 1 \tag{1}$$

where $r(x,t) = \sqrt{[(x-t)^2 + y^2]}$. $U(x)$ is the total fluid velocity on the body surface nondimensionalized by the freestream velocity and t is the location of a unit strength source at an arbitrary location on the body's axis of symmetry. This equation is solved by iteration to minimize an error function within a user-prescribed tolerance (see Albone[12] for details). This method is more rapid than other surface singularity methods, but yields velocity on the body surface only. Within the user-prescribed tolerance the method is exact. The perturbation potential was found by integrating the perturbation velocity, using cubic splines to describe the velocities. Figure 2 shows comparisons between the present method (i.e., Landweber's method) and the results of Vandrey,[13] who used a surface source ring method. A least-square curve fit of the present method's data is also included.

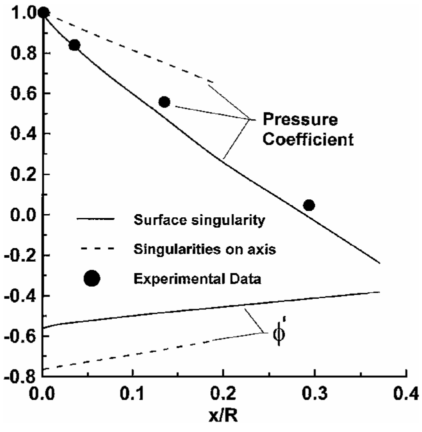

Fig. 1 Effect of singularity location on the perturbation potential and predicted pressure coefficient over a H-C.

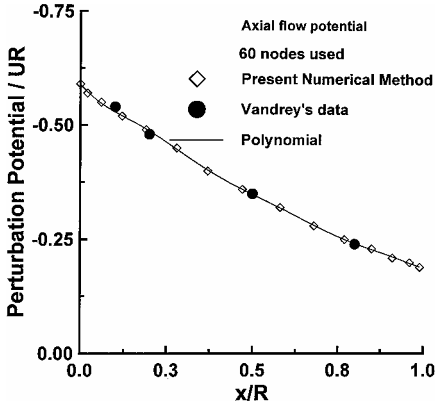

Fig. 2 Predicted axial perturbation potential over a H-C.

Transverse Flow

The transverse flow was solved for using the more general, but computationally more expensive method of Lotz.[11] This method uses an axial distribution of surface source/sink rings in combination with the no penetration boundary condition to determine the source strengths. The method is complicated by the behavior of the kernel or core functions, which are singular when the effect of the element on itself is evaluated, requiring careful implementation of suitable limits. The method consists of calculating the geometric Kernel

$$K^e = 1\Big/\sqrt{(\alpha^2 + K^2)}\left\{G_1(k^2)[(r-\rho) - r'(x-\zeta)] - \rho G_2(k^2)\right\} \tag{2}$$

where G_1 and G_2 are functions of complete elliptic integrals of both the first and second kind:

$$G_1 = \frac{(2-k^2)E(k^2)}{2(1-k^2)} - K(k^2) \tag{3}$$

$$G_2 = 2[(2-k^2)/k^2][E(k^2) - K(k^2)] + [E(k^2) - K(k^2)] \tag{4}$$

with

$$K(k^2) = \int_0^{\pi/2} \frac{\mathrm{d}z}{\sqrt{1 - k^2 \sin^2 z}}$$

elliptic integral of the first kind

$$E(k^2) = \int_0^{\pi/2} \sqrt{1 - k^2 \sin^2 z}\,\mathrm{d}z$$

elliptic integral of the second kind α, ρ, k, K, x, ζ, and r are geometric parameters given by

$$\alpha^2 = (x-\zeta)^2 + r^2 + \rho^2 \qquad \underline{k}^2 = 2r\rho \tag{5a}$$

$$\lambda^2 = \frac{\alpha^2 - \underline{k}^2}{\alpha^2 + \underline{k}} \qquad k^2 = 1 - \lambda^2 \tag{5b}$$

The method then consists of solving for each $P(x,r)$ by varying the running point $RP(\zeta,\rho)$, taking care to evaluate $P = RP$ so as to avoid a singular solution (caused by the elliptic integral G1), (see Fig. 3) where

$$P_n(x,r) = \int_0^l \frac{P_{n-1}(\zeta,\rho)K^e}{\rho}\,\mathrm{d}\zeta \qquad P_1(x,r) = \int_0^l K^e\,\mathrm{d}\zeta \tag{6}$$

The solutions of the preceding equations are then combined in a rising power series of π for the source ring strengths at any fixed point location:

$$f^e(x,r) = f_0^e(x,r)$$

$$- \frac{f_0^e(x,r)}{r}\left[\frac{P_1(x,r)}{\pi} - \frac{P_2(x,r)}{\pi^2} + \frac{P_3(x,r)}{\pi^3} - \cdots\right] \tag{7}$$

Finally, the perturbation potential at any point in the flowfield is found using

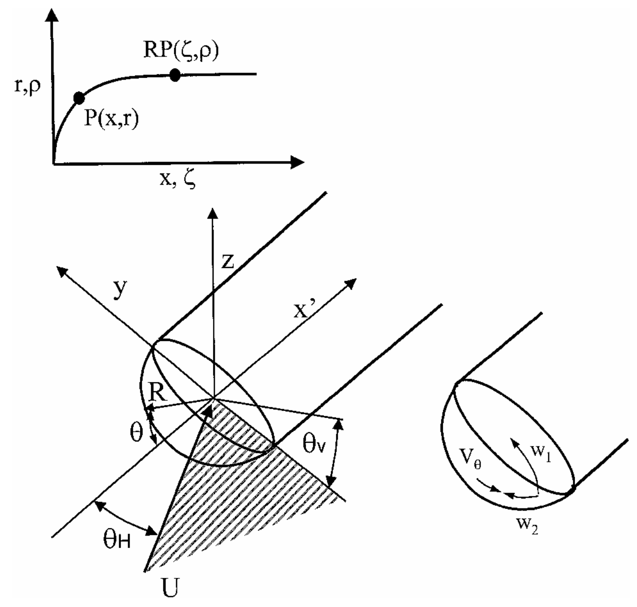

Fig. 3 Theoretical development geometric variables and calculated velocity components.

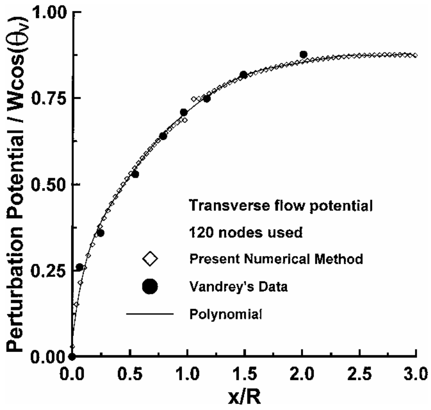

Fig. 4 Predicted transverse perturbation potential over a H-C.

$$\phi' = -4W\cos\theta_V \int_0^l \frac{f^e(\zeta,\rho)}{\sqrt{\alpha^2 + k^2}} \sqrt{1+\rho'^2}\, G_3(k^2)\rho\, \mathrm{d}\zeta \tag{8}$$

where W is the transverse velocity, G_3 is a function of complete elliptic integrals of the first and second kind, i.e.,

$$G_3 = 1/k^2[(2 - k^2)K(k^2) - 2E(k^2)] \tag{9}$$

Although tedious, the method does yield essentially exact solutions. Figure 4 shows comparisons of the transverse potential between the present method and the results of Vandrey,[13] who used a surface source ring method. A polynomial curve fit is also presented.

Prediction of Pressures

Using the axial and transverse perturbation potentials determined using the preceding surface singularity methods allows the determination of the attached flow surface pressures at any location on the H-C as will be detailed. As already mentioned the contributions of the axial and transverse flow can be determined separately as a result of the linear nature of Laplaces' equation.

Velocity Caused by Axial Flow: $0 < x/R < 1$

Figure 3 shows the variables used in the present development. For utility the formulation uses the position variable θ for location over the hemisphere body (rather than x/R). A least-squares curve fit of the perturbation potential in Fig. 2 yields, using $x/R = 1 - \cos(\theta)$ with $x' = x - R$ (after some manipulation):

$$\begin{aligned}\phi' = UR\cos(\theta_H)\{&\sin(\theta)[0.1375 - 0.0744\cos(\theta)\\ &- 0.1869\cos^2(\theta) - 0.0457\cos^3(\theta) + 0.1276\cos^4(\theta)\\ &+ 0.06404\cos^5(\theta) - 0.0608\cos^6(\theta) - 0.0658\cos^7(\theta)\\ &- 0.0220\cos^8(\theta) - 0.0026\cos^9(\theta)] + 0.1650\theta - 0.59\}\end{aligned} \tag{10}$$

The tangential velocity is then

$$V_\theta = \frac{1}{R}\frac{\partial\phi_{\mathrm{tot}}}{\partial\theta} \tag{11}$$

where ϕ_{tot} is the freestream potential $[= -UR\cos(\theta)\cos(\theta_H)]$ plus the perturbation potential. Evaluation yields, where $U\cos(\theta_H)\sin(\theta)$ is the freestream contribution,

$$\begin{aligned}V_\theta = U\cos(\theta_H)[&\sin(\theta) + 0.5115\cos(\theta) - 0.0115\cos^2(\theta)\\ &- 1.0714\cos^3(\theta) - 0.5032\cos^4(\theta) + 1.003\cos^5(\theta)\\ &+ 0.8445\cos^6(\theta) - 0.2496\cos^7(\theta) - 0.5029\cos^8(\theta)\\ &- 0.1982\cos^9(\theta) - 0.026\cos^{10}(\theta) + 0.2394]\end{aligned} \tag{12}$$

Velocity Caused by Transverse Flow: $0 < x/R < 1$

The calculation of the induced velocities as a result of the transverse component of the decomposed freestream is straightforward but contains a subtlety. The transverse flow induces two velocity components on the hemisphere surface: one lateral w_1 and one axial w_2 such that it opposes the velocity caused by axial decomposition of the freestream. It is this component w_2 that is responsible for the rearward movement of the attachment line stagnation point with incidence.

Using the numerical data in Fig. 4 gives a transverse perturbation potential of

$$\begin{aligned}\phi' = UR\sin(\theta_H)\cos(\theta_V)[&0.7146 - 0.2789\cos(\theta) - 0.1396\cos^2(\theta)\\ &- 0.0802\cos^3(\theta) - 0.1802\cos^4(\theta) + 0.1363\cos^5(\theta)\\ &+ 0.4177\cos^6(\theta) + 0.0194\cos^7(\theta) - 0.3272\cos^8(\theta)\\ &- 0.2033\cos^9(\theta) - 0.0369\cos^{10}(\theta)]\end{aligned} \tag{13}$$

The lateral velocity component is found using

$$w_1 = \frac{1}{R}\frac{\partial\phi_{\mathrm{tot}}}{\partial\theta_V} \tag{14}$$

where ϕ_{tot} is the freestream potential $[= UR\cos(\theta_V)\sin(\theta_H)\sin(\theta)]$ plus the perturbation potential. Evaluation yields

$$\begin{aligned}w_1 = -U\sin(\theta_H)\sin(\theta_V)[&0.7146 - 0.2789\cos(\theta)\\ &- 0.1396\cos^2(\theta) - 0.0802\cos^3(\theta) - 0.1802\cos^4(\theta)\\ &+ 0.1363\cos^5(\theta) + 0.4177\cos^6(\theta) + 0.0194\cos^7(\theta)\\ &- 0.3272\cos^8(\theta) - 0.2033\cos^9(\theta)\\ &- 0.0369\cos^{10}(\theta) + \sin(\theta)]\end{aligned} \tag{15}$$

The axial component w_2 is determined using

$$w_2 = \frac{1}{R}\frac{\partial\phi_{\mathrm{tot}}}{\partial\theta} \tag{16}$$

Evaluation of w_2 gives

$$\begin{aligned}w_2 = U\sin(\theta_H)\cos(\theta_V)[&0.2407\cos^2(\theta)\sin(\theta)\\ &+ 0.7208\cos^3(\theta)\sin(\theta) - 0.6815\cos^4(\theta)\sin(\theta)\\ &- 2.5059\cos^5(\theta)\sin(\theta) - 0.1355\cos^6(\theta)\sin(\theta)\\ &+ 0.2793\cos(\theta)\sin(\theta) + 0.2789\sin(\theta) + \cos(\theta)\\ &+ 2.6179\cos^7(\theta)\sin(\theta) + 1.8297\cos^8(\theta)\sin(\theta)\\ &+ 0.3698\cos^9(\theta)\sin(\theta)]\end{aligned} \tag{17}$$

The surface pressure coefficient is then found using

$$C_P = 1 - \left[(V_\theta - w_2)^2 + w_1^2\right] / U^2 \tag{18}$$

Surface Velocities: 1 < *x*/*R* < 2

A similar procedure is used for the afterbody, noting that for this region, $w_2 = \partial\phi_{\text{tot}}/\partial x$ and $V_\theta = \partial\phi_{\text{tot}}/\partial x$. The resulting expressions for the three velocity components are

$$\begin{aligned} V_\theta = U\cos(\theta_H)\Bigg[& 0.0359 + \frac{x}{R}2.4668 - \left(\frac{x}{R}\right)^2 11.1589 \\ & + \left(\frac{x}{R}\right)^3 32.7894 - \left(\frac{x}{R}\right)^4 57.1212 + \left(\frac{x}{R}\right)^5 58.7740 \\ & - \left(\frac{x}{R}\right)^6 37.0220 + \left(\frac{x}{R}\right)^7 14.4878 - \left(\frac{x}{R}\right)^8 3.4418 \\ & - \left(\frac{x}{R}\right)^9 0.4549 - 0.0257\left(\frac{x}{R}\right)^{10} + 1\Bigg] \end{aligned} \tag{19}$$

$$\begin{aligned} w_1 = -U\sin(\theta_H)\sin(\theta_V)\Bigg[& 0.0141 + \frac{x}{R}3.0142 - \left(\frac{x}{R}\right)^2 11.5727 \\ & + \left(\frac{x}{R}\right)^3 30.2474 - \left(\frac{x}{R}\right)^4 48.8443 + \left(\frac{x}{R}\right)^5 50.2109 \\ & - \left(\frac{x}{R}\right)^6 33.4521 + \left(\frac{x}{R}\right)^7 14.3547 - \left(\frac{x}{R}\right)^8 3.8209 \\ & + \left(\frac{x}{R}\right)^9 0.5731 - \left(\frac{x}{R}\right)^{10} 0.0369 + 1\Bigg] \end{aligned} \tag{20}$$

$$\begin{aligned} w_2 = U\cos(\theta_V)\sin(\theta_H)\Bigg[& 3.0142 - \frac{x}{R}23.1454 + \left(\frac{x}{R}\right)^2 90.7422 \\ & - \left(\frac{x}{R}\right)^3 195.3772 + \left(\frac{x}{R}\right)^4 251.0545 - \left(\frac{x}{R}\right)^5 200.7126 \\ & + \left(\frac{x}{R}\right)^6 100.4829 - \left(\frac{x}{R}\right)^7 30.5675 + \left(\frac{x}{R}\right)^8 5.1577 \\ & - \left(\frac{x}{R}\right)^9 0.3698\Bigg] \end{aligned} \tag{21}$$

As before, pressures on the cylinder are estimated by substituting Eqs. (19–21) into Eq. (18).

Experimental Equipment and Procedure

The wind-tunnel model was manufactured from aluminum. Relevant dimensions are shown in Fig. 5. The H-Cs diameter was 1.5 in. (38.1 mm) to accommodate the pressure tappings. The hemisphere had 25 tappings in three rows of eight (spaced 20 deg apart) in addition to a center tap. The pressure ports were spaced at $\Delta\theta = 10$-deg intervals along the periphery of the nose. The internal diameter of the tappings was 0.01 in. (0.25 mm). The tappings were as small as possible to minimize their effect on the flow. To determine the length of the H-C such that the influence of its blunt base would be minimized, numerical experiments were undertaken to determine the effect of a blunt aft portion. The simulation was conducted using the surface vortex ring method to simulate the axial flow and a surface source ring method to simulate the transverse flow, as just described. The numerical data suggested that the effects of the cylinder base (on the hemisphere) were minimal for base locations greater than six cylinder diameters from the front of the model. The model was attached to a pitching mechanism to allow accurate incidence variation of the model from 0 to 45 deg. The model could be set to θ_H within 0.05 deg of the required value.

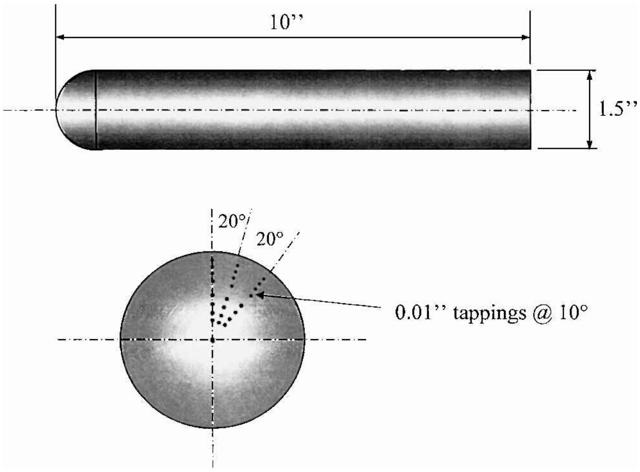

Fig. 5 Wind-tunnel model details.

The tests were undertaken in the Texas A&M University 3 × 4 ft continuous wind tunnel at velocities of 10.4 and 20.5m/s, corresponding to $Re = 2.6 \times 10^4$ and 5.3×10^4 based on the diameter of the H-C. At these velocities the turbulence intensity is typically < 0·3%. The wind-tunnel jet velocity uniformity is typically within 0.1%. The tunnel has active cooling and is normally maintained at 20°C for the duration of a run.

Pressures were recorded using an ESP 32-port electronic pressure scanner with a range of ±2500 Pa. The signals from the ESP were digitized using a 12-bit A/D board giving a resolution of ±0·24% of full scale. The A/D's sampling frequency was 5kHz. The ESP was monitored using a factory calibrated Air Neotronics digital micromanometer with a resolution of 0.1 Pa. Before each test, the ESP was recalibrated to reduce errors. Repeated data runs yielded an estimated uncertainty of the data of 0.3% of full scale for a 95% (2σ) confidence interval. During the testing, after the model was pitched to a new incidence approximately 10–15s was allowed to elapse to allow the pressures to reach their steady-state values. The model was pitched through 0, 15, 30, and 45 deg. At each θ_H the ESP was sampled 200 times and averaged. No corrections to account for wall effects, i.e., solid and wake blockage, were applied to the data, as a large majority of the test cases would encompass significant extents of separated flow making accurate application of corrections uncertain. Furthermore, for the worst-case scenario $\theta_H = 45$ deg, the combined blockage of the model, and mount is less than 1.4% suggesting that wall effects would be negligible.

Comparisons with Theory

Predictions of the surface pressure coefficient measured over a H-C at zero incidence using Landwebers[10] method and Eq. (18) are shown in Fig. 6. Agreement with the present experimental data is seen to be good. Also included in the figure is the potential solution for the flow over a sphere $[= 1 - 9/4\sin^2(\theta)]$ as well as an empirical modification to this formula to account for the effect of the cylinder on the hemisphere $[= 1 - 2.07\sin^2(\theta)]$. As noted prior, for $\theta = \pm 15$ deg the presence of the cylinder has a negligible effect on the hemisphere surface pressure. For greater x/R the cylinder acts as a downstream source, retarding the surface velocities thus causing comparatively higher surface pressures. The empirical relation is seen to accurately estimate the surface pressures over the forward $\theta = 55$ deg of the hemisphere.

Hoang[1] performed a comprehensive study on the behavior of a H-C at incidence. His data included surface pressure, surface flow topology, as well as hot wire and laser Doppler velocimetry measurements. Consequently, Hoang's data ($Re = 4.2 \times 10^4$), in addition to

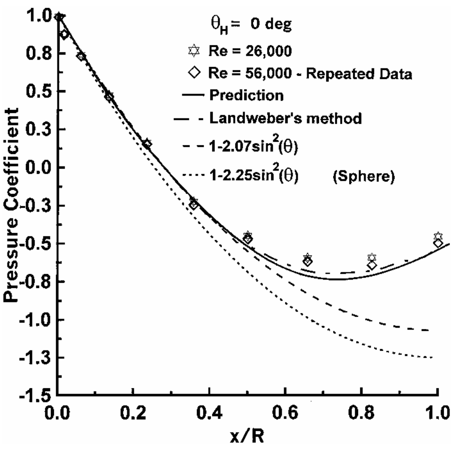

Fig. 6 Predicted surface pressure coefficient over a H-C, θ_H = 0 deg. Present experimental data.

the present experimental effort, will be used for prediction validation. To correctly evaluate the potential of the present expression, it is necessary to know its natural limitations following from the unique inherent viscous characteristics of a H-C. Consequently, these characteristics/flow behaviors will be discussed briefly, although touched upon in the Introduction. At the Reynolds-number range of the experimental data included in this study, the surface flow displays a marked and systematic variation with θ_H as elucidated by Hoang.[1] At zero incidence surface skin-friction patterns indicate the existence of an axisymmetrical closed separation bubble (as mentioned prior) propagating from the H-C juncture. Incidence causes an asymmetry of this bubble with a leeward displacement of the separation borders. Increasing θ_H to 10 deg sees the formation of two horn vortices (representing unstable foci) from the upper lateral edges of the bubble at $\theta_V \approx \pm 130$ deg. Two symmetric crossflow separation lines are also apparent on the cylinder at this incidence and indicate the possible existence of leeward vortices. These separation lines are clearly distinct from the horn vortices and originate approximately $2R$ aft of the horn vortices. Increasing incidence shows a leeward displacement of the separation region located at the H-C juncture. Skin-friction patterns from Hoang[1] are reproduced in Figs. 7b and 7c representing the H-C at $\theta_H = 20$ deg, as this is the incidence of most of the data comparisons presented in this study. A summary of the surface flow features is also presented (Fig. 7a). The crossflow separation line is clearly seen running along the side edge of the cylinder. This separation point is seen to move progressively windward with increasing x/R. A trace of the surface's pressures experienced along a skin-friction line originating from $x/R = 1$, $\theta_V = 0$ deg, and $x/R = 5$, $\theta_V = 0$ showed that the movement of this separation line to smaller θ_V (i.e., windward) with increasing x/R is not caused by a more favorable pressure distribution downstream (the large x/R pressure distributions are more favorable). The trajectory of this separation line is thus probably caused by the increasing boundary-layer thickness downstream increasing the tendency for separation. Two darker lines running over the top of the H-C are identified as vortex induced separation lines, suggesting the presence of two vortices per side—a primary and secondary separation vortex. The primary vortex causes the secondary flow separation. Vortex induced pressure gradients convect fluid laterally outwards under the primary vortex core, such that the fluid encounters an adverse pressure gradient, which causes the boundary layer to separate. The ensuing free shear layer rolls up and forms a vortex of opposite rotation (to the primary). The skin-friction lines emanating from the attachment line are seen to progressively reduce in inclination relative to the body (see Fig. 7c), and at $x/R > 4.8$ they are inclined at 40 deg to the freestream. This condition corresponds to Munk's[14] "2α" type of flow (where local lift development assuming no flow separation is proportional to 2α; here, $\theta_H = \alpha$) and suggests that over this region of the H-C the flow is essentially inviscid. Figure 7d shows a sketch, proposed by Maskell,[15] showing

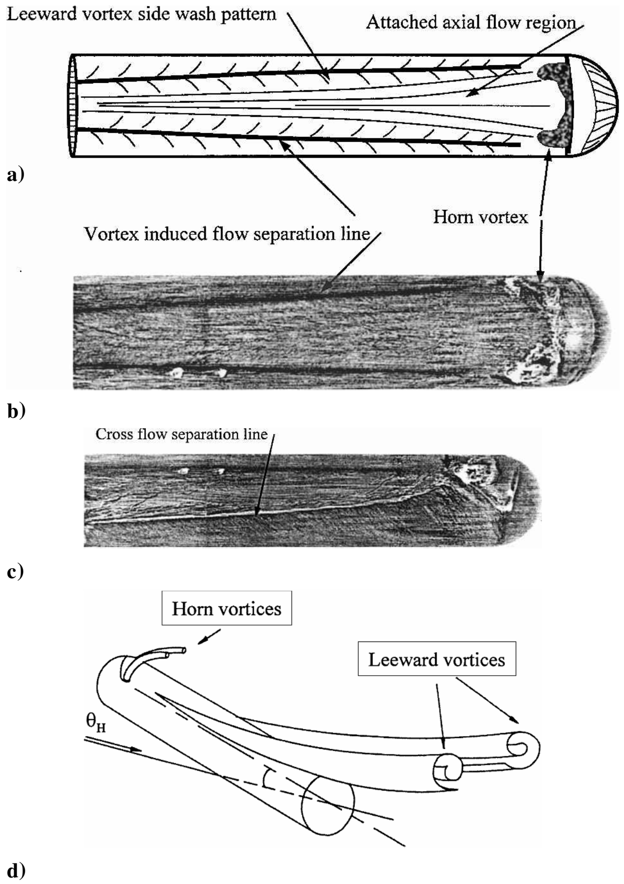

Fig. 7 Flow patterns over a H-C, θ_H = 20 deg: a) Skin-friction pattern summary; b) Surface skin-friction patterns,[1] top view; c) Surface skin-friction patterns,[1] side view; d) Three-dimensional off-surface flow representation[15].

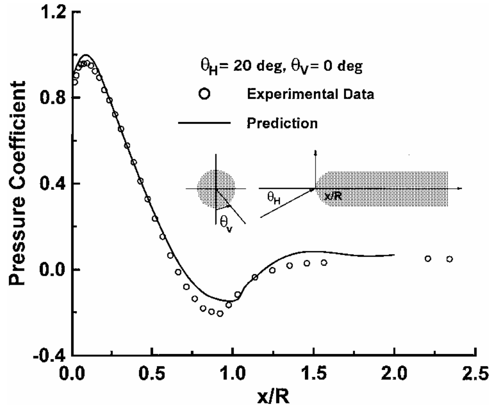

Fig. 8 Comparison of predicted [Eq. (18)] and experimental pressure coefficients over a H-C, θ_H = 20 deg, θ_V = 0 deg. Experimental data from Ref. 1.

a three-dimensional representation of the off-surface flow features just detailed.

Hoang's[1] skin-friction data indicate that the vortex-induced flow separation lines (associated with the leeward vortices) gradually approach the horn vortices, and at $\theta_H \approx 25$ deg these flow features connect. The crossflow separation lines also gradually move toward larger θ_V values (the back of the cylinder) with incidence as the axial surface flow component reduces relative to the transverse (effectively increasing the crossflow Reynolds number). Beyond about 33-deg incidence, the presence of the horn vortices cannot be established.[1]

Theoretical and experimental comparisons for a H-C at 20-deg incidence ($= \theta_H$) are presented in Figs. 8–17. Values for θ_V from

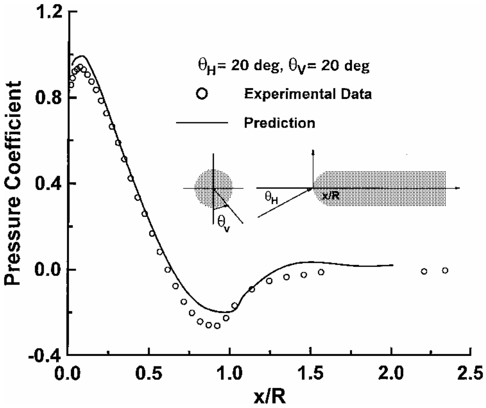

Fig. 9 Comparison of predicted [Eq. (18)] and experimental pressure coefficients over a H-C, $\theta_H = 20$ deg, $\theta_V = 20$ deg. Experimental data from Ref. 1.

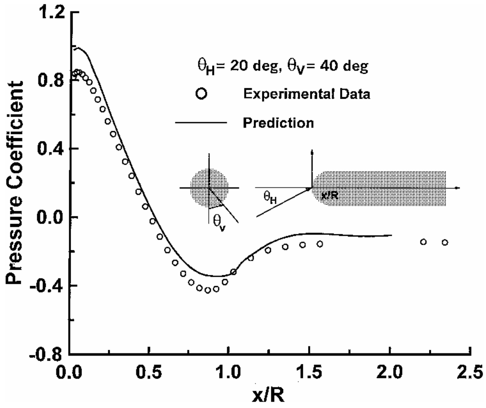

Fig. 10 Comparison of predicted [Eq. (18)] and experimental pressure coefficients over a H-C, $\theta_H = 20$ deg, $\theta_V = 40$ deg. Experimental data from Ref. 1.

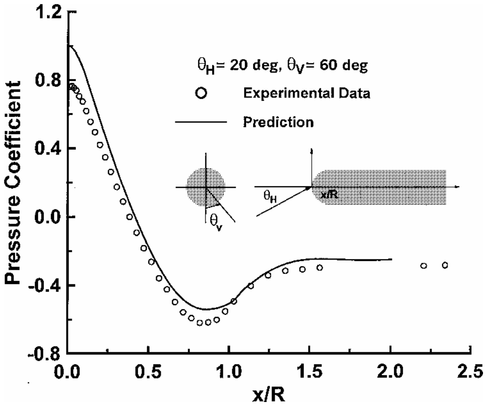

Fig. 11 Comparison of predicted [Eq. (18)] and experimental pressure coefficients over a H-C, $\theta_H = 20$ deg, $\theta_V = 60$ deg. Experimental data from Ref. 1.

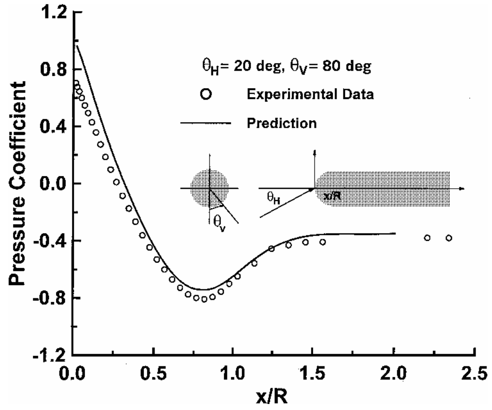

Fig. 12 Comparison of predicted [Eq. (18)] and experimental pressure coefficients over a H-C, $\theta_H = 20$ deg, $\theta_V = 80$ deg. Experimental data from Ref. 1.

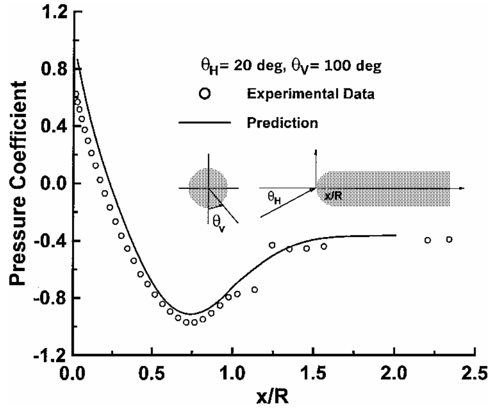

Fig. 13 Comparison of predicted [Eq. (18)] and experimental pressure coefficients over a H-C, $\theta_H = 20$ deg, $\theta_V = 100$ deg. Experimental data from Ref. 1.

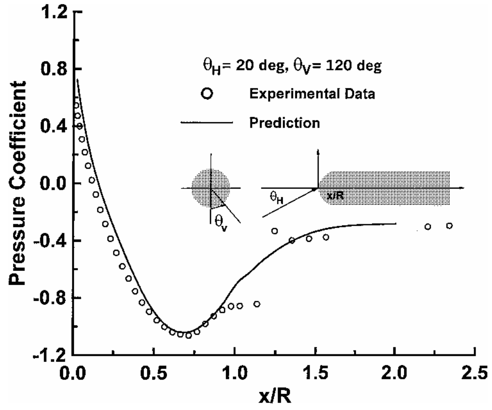

Fig. 14 Comparison of predicted [Eq. (18)] and experimental pressure coefficients over a H-C, $\theta_H = 20$ deg, $\theta_V = 120$ deg. Experimental data from Ref. 1.

0 to 180 in 20-deg increments are presented to clearly demonstrate the accuracy of the predictions [i.e., Eq. (18)] as the flow develops. Figure 8 shows predictions of the surface pressure coefficient along the attachment line. Good agreement over the forward envelope of the cylinder is seen. The minimum recorded pressures are somewhat underpredicted. The pressure recovery region is relatively well captured. Downstream pressures on the cylinder ($x/R > 1.5$) are well approximated. Although the location of the minimum pressure region is predicted slightly too far aft, the form of the theoretical distribution, with a sharp pressure recovery following the suction peak, is representative.

Similar trends are seen in Fig. 9 ($\theta_V = 20$ deg). Increasing θ_V to 40 deg, Fig. 10 shows an overprediction and underprediction respectively of the maximum and minimum measured pressures, although the general form of the pressure distribution is well captured as are the afterbody pressures. $\theta_V = 60$ deg shows similar characteristics (see Fig. 11). Increasing θ_V beyond 60 deg (Fig. 12) shows good correlation of predicted pressures with experiment, except for small x/R where pressures are overpredicted. Pressures on the cylinder afterbody are well captured. Also note that the x/R location of the minimum pressure is more accurately captured than for lower θ_V, where the predicted minimum pressures are further aft than that of the experiment data. Increasing θ_V shows increasing dominance of the crossflow w_1 velocity term [$\propto \sin(\theta_V)$] and a reduction in the w_2 [$\propto \cos(\theta_V)$] term, which opposes V_θ.

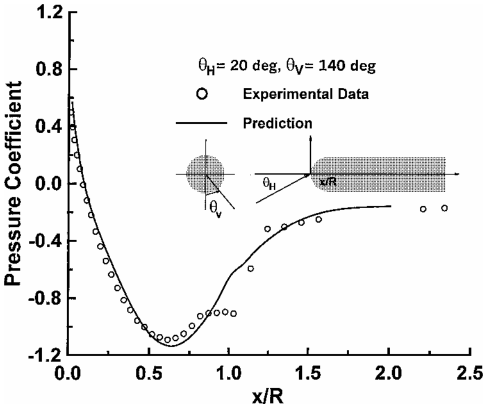

Fig. 15 Comparison of predicted [Eq. (18)] and experimental pressure coefficients over a H-C, θ_H = 20 deg, θ_V = 140 deg. Experimental data from Ref. 1.

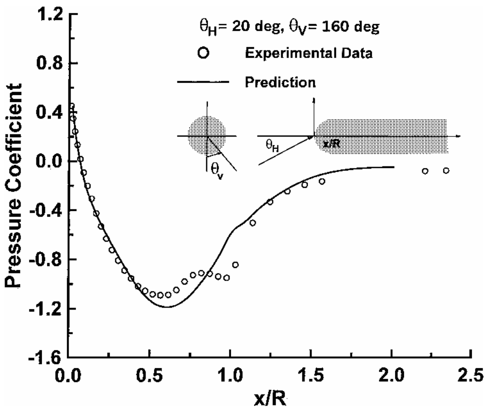

Fig. 16 Comparison of predicted [Eq. (18)] and experimental pressure coefficients over a H-C, θ_H = 20 deg, θ_V = 160 deg. Experimental data from Ref. 1.

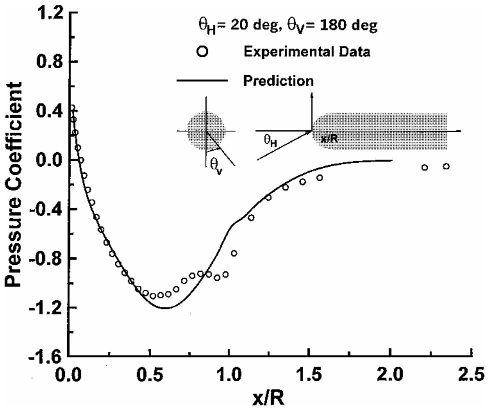

Fig. 17 Comparison of predicted [Eq. (18)] and experimental pressure coefficients over a H-C, θ_H = 20 deg, θ_V = 180 deg. Experimental data from Ref. 1.

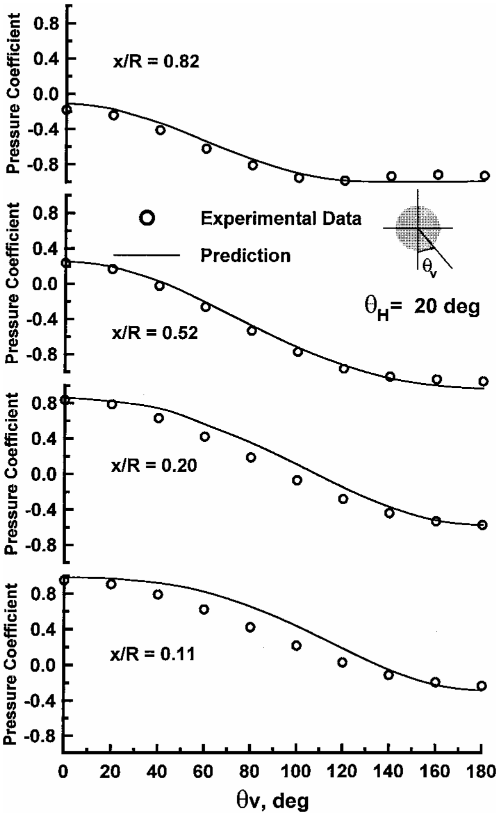

Fig. 18 Effect of θ_V on predicted [Eq. (18)] and experimental surface pressure coefficients, θ_H = 20 deg. Experimental data from Ref. 1.

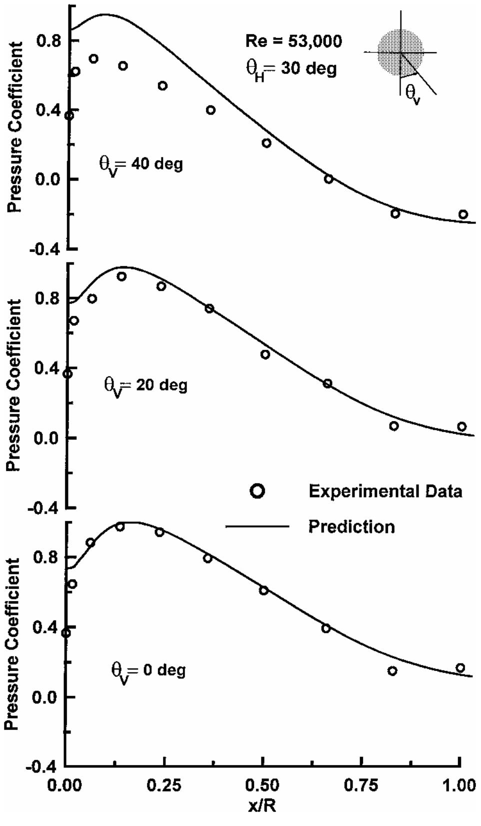

Fig. 19 Effect of θ_V on predicted [Eq. (18)] and experimental surface pressure coefficients, θ_H = 30 deg. Present experimental data.

For $\theta_V > 90$ deg the experimental data show evidence of separation effects ($x/R \approx 1{\cdot}25$, see Fig. 13), with Hoang's[1] data indicating the presence of a closed separation bubble laterally terminating in two horn vortices (see Fig. 7). These flow effects are viscous in origin and could not be captured by the present inviscid method. The form of the pressure distribution, i.e., flat, between $1{\cdot}25 < x/R < 1{\cdot}6$ is clearly that of a closed separation bubble (despite the horn vortices). However, for $\theta_V \leq 140$ deg pressures over the forward region of the hemisphere as well as the minimum pressure region are well estimated (Figs. 13–15) as are the final afterbody pressures. Examination of Figs. 8–15 indicates that Eq. (18) describes the changing form of the pressure recovery region well, from a sharp initial

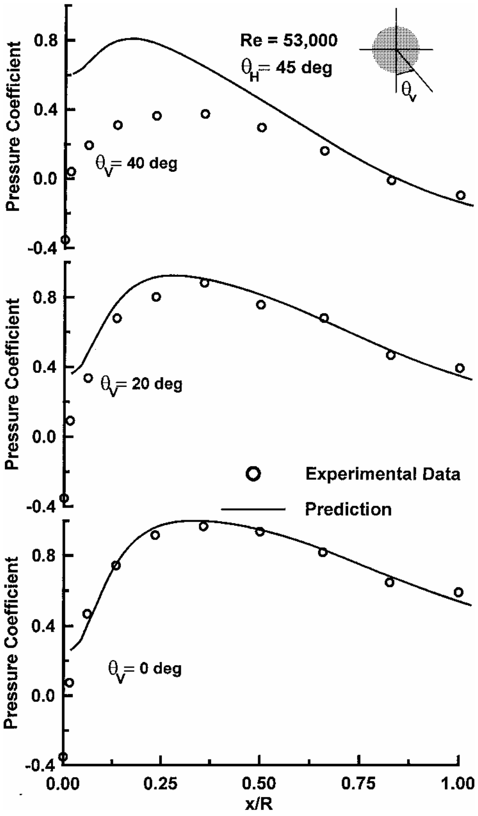

Fig. 20 Effect of θ_V on predicted [Eq. (18)] and experimental surface pressure coefficients, θ_H = 45 deg. Present experimental data.

recovery following the point of minimum pressure for small θ_V (see Figs. 8–10) to a milder recovery (Figs. 11–15) for larger θ_V.

For $\theta_V = 160$ and 180 deg (Figs. 16 and 17) pressures over the forward portion of the hemisphere are still well captured ($\theta < 55$ deg). Interestingly, pressures over the cylinder are well estimated despite the presence of separated flow. This is probably caused by the mutual downwash from the leeward vortices creating a region of attached flow between them, which is approximately potential, as is also seen in delta wings at moderate angles of attack.

It is instructive to explicitly investigate the ability of the theory to predict pressure as a function of θ_V at a particular axial location. These data are presented in Fig. 18 along with data from Hoang.[1] The predictions faithfully capture the magnitude and dependence of the pressure coefficient on θ_V although accuracy improves for larger x/R. Comparisons of the method with the current experimental data at higher incidence $\theta_H = 30$ and 45 deg are presented in Figs. 19 and 20. Even at these extreme incidences, close accord is demonstrated for moderate θ_V (<40 deg).

The experimental data used for comparison in this study were acquired at relatively low Reynolds numbers, which may cast doubt as to the validity of the comparisons at higher Reynolds numbers. However, the theoretical development is inviscid and thus would be representative for higher Reynolds-number flows.

Conclusions

Given the widespread application of the hemisphere-cylinder configuration, it would be of great utility for conceptual design purposes to have a simple, analytical expression to estimate surface pressures. Such an expression would also allow an appreciation for the magnitude and relative effect of the design variables.

Consequently, a potential flow-based equation was developed to estimate the surface pressures over a hemisphere-cylinder. The expression used least-square regression curve fits of numerically generated axial and transverse perturbation potentials. These potentials were calculated using surface singularity methods. Numerous comparisons of surface pressure estimates using the resulting expression with experimental data are presented. The equation showed the ability to closely predict incidence effects on pressure around the hemisphere cylinder's surface.

References

[1] Hoang, H. T., "The Hemisphere-Cylinder at an Angle of Attack," Ph.D. Dissertation, Dept. of Engineering Mechanics, Virginia Polytechnic Inst., and State Univ., Blacksburg, VA, Dec. 1991.

[2] Meade, A. J., and Schiff, L. B., "Experimental Study of Three Dimensional Separated Flow Surrounding a Hemisphere-Cylinder at Incidence," AIAA Paper 87-2492-CP, Aug. 1987.

[3] Meier, H. U., and Kreplin, H. P., "Experimental Investigations of Boundary Layer Transition and Separation on a Body of Revolution," *Zeitschrift für Flugwiss Weltraumforschung*, Vol. 4, 1980, pp. 65–71.

[4] Ying, S. X., Schiff, L. B., and Steger, J. L., "A Numerical Study of Three Dimensional Separated Flow Past a Hemisphere Cylinder," AIAA Paper 87-1207, June 1987.

[5] Schlichting, H., *Boundary-Layer Theory*, 7th ed., McGraw–Hill, New York, 1979, pp. 20–33.

[6] Traub, L. W., "Prediction of Tunnel Wall Upwash for Delta Wings Including Vortex Breakdown Effects," *The Aeronautical Journal*, Vol. 103, No. 1021, 1999, pp. 139–142.

[7] Traub, L. W., "Prediction of Vortex Breakdown and Longitudinal Characteristics of Swept Slender Planforms," *Journal of Aircraft*, Vol. 34, No. 3, 1997, pp. 353–359.

[8] Traub, L. W., "Prediction of Delta Wing Leading Edge Vortex Circulation and Lift-Curve Slope," *Journal of Aircraft*, Vol. 34, No. 3, 1997, pp. 450–452.

[9] Traub, L. W., "A Theoretical and Experimental Investigation of Biplane Delta Wings," *Journal of Aircraft*, Vol. 38, No. 3, 2001, pp. 536–546.

[10] Landweber, L., "The Axially Symmetric Potential Flow About Elongated Bodies of Revolution," Rept. Taylor Model Basin, Washington, No. 761, March 1951.

[11] Lotz, I., "Calculation of Potential Flow Past Airship Bodies in Yaw," NACA TM 675, July 1932.

[12] Albone, C. M., "Fortran Programmes for Axisymmetric Potential Flow Around Closed and Semi-Infinite Bodies," Aeronautical Research Cauncil, C.P. 1216, London, March 1972.

[13] Vandrey, F., "A Method for Calculating the Pressure Distribution of a Body of Revolution Moving in a Circular Path Through a Perfect Incompressible Fluid," Aeronautical Research Council, R&M 3139, London, Dec. 1953.

[14] Munk, M. M., "Airship Theory," NACA Repts. 184 and 191, 1923/24.

[15] Maskell, E. C., "Flow Separation in Three Dimensions," Royal Aircraft Establishment, Rept. 2565, Nov. 1955.